Journal of Hematology & Oncology

RESEARCH

Open Access

Anti-TGF-β/PD-L1 bispecific antibody synergizes with radiotherapy to enhance antitumor immunity and mitigate radiation-induced pulmonary fibrosis

Yuze Wu[1], Yuheng Yan[1], Yarong Guo[2], Mengke Niu[1], Binghan Zhou[1], Jing Zhang[3], Pengfei Zhou[3], Qian Chu[1], Qi Mei[1,2*], Ming Yi[4*] and Kongming Wu[2,5*]

Abstract

Background Despite the success of immune checkpoint inhibitors (ICIs) in multiple malignant tumors, a significant proportion of patients remain unresponsive to treatment. Radiotherapy (RT) elicits immunogenic antitumor responses but concurrently activates several immune evasion mechanisms. Our earlier research demonstrated the efficacy of YM101, an anti-TGF-β/PD-L1 bispecific antibody, in stroma-rich tumors. Nevertheless, YM101 has demonstrated reduced effectiveness in non-inflamed tumors characterized by poor immune cell infiltration. This study investigated the potential synergy between RT and YM101 in overcoming immunotherapy resistance and mitigating RT-induced pulmonary fibrosis.

Methods The antitumor activity and survival outcomes of RT plus YM101 treatment in vivo were explored in several non-inflamed murine tumor models. Furthermore, the inhibition of pulmonary metastases was assessed in a pulmonary metastasis model. The impact of RT on dendritic cell (DC) maturation was quantified by flow cytometry, whereas cytokine and chemokine secretions were measured by ELISA. To comprehensively characterize changes in the tumor microenvironment, we utilized a combination of methods, including flow cytometry, IHC staining, multiplex inmunofluorecence and RNA sequencing. Additionally, we evaluated the impact of YM101 on RT-induced pulmonary fibrosis.

Results RT plus YM101 significantly inhibited tumor growth, prolonged survival and inhibited pulmonary metastases compared with monotherapies in non-inflamed tumors with poor immune infiltration. RT promoted DC maturation in a dose-dependent manner and increased the secretions of multiple proinflammatory cytokines. Mechanistically, RT plus YM101 simultaneously increased the infiltration and activation of intratumoral DCs and tumor-infiltrating

*Correspondence:
Qi Mei
borismq@163.com
Ming Yi
mingyi_onco@outlook.com
Kongming Wu
wukm_lab@163.com

Full list of author information is available at the end of the article

lymphocytes and reshaped the tumor microenvironment landscape. Notably, YM101 attenuated both RT-induced peritumoral fibrosis and pulmonary fibrosis.

Conclusions Our findings suggest that RT combined with YM101 enhances antitumor immunity and overcomes resistance in non-inflamed tumors in preclinical models, while simultaneously showing potential in mitigating RT-induced fibrosis. This combination therapy demonstrates promise in overcoming ICI resistance, while potentially sparing normal pulmonary tissue, thereby providing a strong rationale for further clinical investigations.

Keywords Radiotherapy, PD-L1, TGF-β, Bispecific antibody, Tumor microenvironment

Background

Over the past two decades, the paradigm of malignant tumor treatment has been revolutionized, which has been predominantly achieved by the advent of immune checkpoint inhibitors (ICIs) [1–4]. Despite the approval of numerous ICIs for a variety of malignancies, a majority of patients exhibit limited or no response to immunotherapy, especially ICI monotherapy [5–7], thereby necessitating solutions to address poor response rates and acquired resistance issues.

The complex framework of cancer cells, infiltrating and resident immune cells, stromal cells, soluble factors, and the extracellular matrix is collectively termed the tumor microenvironment (TME) [8, 9]. Tumors are typically categorized into three main immunophenotypes: immune-inflamed, immune-excluded, and immune-desert phenotypes [10, 11]. The latter two types, which are often referred to as non-inflamed tumors, are resistant to ICIs, which has been increasingly attributed to the complex interaction of immunosuppressive factors within the TME [12]. Among these factors, transforming growth factor-β (TGF-β) has emerged as a critical molecule affecting cancer activities [13, 14]. TGF-β, a pleiotropic cytokine, exerts multiple effects, including the suppression of T cell function, the promotion of regulatory T cell (Treg) differentiation, and the enhancement of cancer-associated fibroblast (CAF) activity [15, 16]. Our previous research focusing on YM101 (a bispecific antibody that simultaneously targets PD-L1 and TGF-β) demonstrated enhanced efficacy compared with monotherapies [17]. Multiple independent studies, including our own previous study, have corroborated the superior therapeutic efficacy of therapies that simultaneously target both the PD-L1 pathway and the TGF-β pathway compared with anti-PD-L1 monotherapy [18, 19]. However, non-inflamed tumors, which are characterized by a low tumor mutational burden (TMB), extensive stromal remodeling, and sparse tumor-infiltrating lymphocytes (TILs), remain resistant to these approaches [13, 20].

Non-inflamed tumors typically exhibit deficient innate antitumor immunity, which can be caused by either the complete absence or suppression of this immunity [21]. Effective antitumor responses to treatments require not only the restoration of T cell exhaustion but also the revitalization of innate immunity [22, 23]. The potential of radiotherapy (RT) to convert non-inflamed tumors into "hot" tumors (thereby sensitizing them to immunotherapy in clinical trials) has garnered significant interest [24, 25]. RT induces a multifaceted immunomodulatory response within the TME. Specifically, it promotes immunogenic cell death (ICD) and augments dendritic cell (DC)-mediated antigen presentation, thereby initiating a cascade of events that activate both innate and adaptive immune responses [26]. Additionally, RT increases leukocyte infiltration, expands the T cell repertoire and upregulates the expression of the immune checkpoint PD-L1, which is thought to synergize with ICIs [27, 28].

However, the interaction between RT-induced immunogenic effects and compensatory immunosuppressive mechanisms is complicated. In addition to PD-L1, the immunostimulating effects of RT are often offset by other important immunosuppressive pathways within the TME, such as the TGF-β pathway [29, 30]. Overall, we presume that RT synergizes with YM101 to enhance antitumor efficacy and overcome resistance in non-inflamed tumors.

Moreover, concerns regarding treatment-related adverse effects, particularly radiation-induced pulmonary fibrosis (RIPF), associated with immunotherapy have increased. Clinical observations have indicated an increased incidence of RIPF in patients with non-small cell lung cancer (NSCLC) who receive anti-PD-L1 as consolidation treatment following chemoradiotherapy [31, 32]. RIPF significantly reduces the quality of life of patients and even causes life-threatening respiratory failure [33]. Currently, there are few effective treatments for RIPF [34]. Given the central role of TGF-β in fibrosis progression [15] and the demonstrated efficacy of TGF-β blockade in ameliorating fibrosis across various pathological models [34, 35], YM101 may mitigate the incidence of RIPF.

In this context, our study investigated the potential of combining RT with YM101 to synergistically enhance antitumor immunity in non-inflamed tumors. We hypothesize that this approach may effectively modulate the TME, thereby overcoming resistance in non-inflamed tumors while simultaneously mitigating RIPF.

By addressing both the efficacy and safety aspects of combined therapy, we aim to provide a novel therapeutic strategy that could expand the benefits of immunotherapy to a broader patient population, thereby potentially transforming the treatment landscape for currently refractory tumors.

Materials and methods

Cell lines and therapeutic antibodies (Abs)

The 4T1 and CT26 cell lines were obtained from the American Type Culture Collection (ATCC). The MC38 cell line was purchased from Annoron Biotechnology Co., Ltd. (Beijing, China). 4T1 and CT26 cells were cultured in RPMI-1640 medium containing 10% FBS. MC38 cells were cultured in DMEM supplemented with 10% FBS.

The Abs, including isotype, anti-TGF-β, anti-PD-L1 and YM101, were obtained from Wuhan YZY Biopharma Co., Ltd., (Wuhan, China) as previously described [17, 36].

Radiotherapy (RT)

Prior to RT, the mice were anesthetized with pentobarbital sodium (15 mg/mL) and secured in a supine position to optimize exposure of the target area. Radiation was delivered using an Elekta Precise clinical linear accelerator (Stockholm, Sweden) with 6-MV X-ray beams (600 cGy/min, source-to-surface distance of 100 cm). Dosimetry verification was performed using a three-dimensional water scanning system to ensure accurate dose delivery. For localized tumor irradiation, a single dose of either 8–10 Gy was precisely delivered to the tumor site, with lead shielding (8 mm thickness) protecting the surrounding normal tissues. Customized tissue-compensating boluses (5 mm) were implemented to ensure dose homogeneity. For the RIPF experiments a single fraction of 20 Gy was administered to target the geometric center of the lung field. The radiation field was collimated to encompass the entire thorax, whereas the head, neck and abdomen were protected using custom-designed lead shielding.

Murine tumor models and treatments

Female BALB/c and C57BL/6 mice (aged 6–8 weeks) were acquired from Beijing Vital River Laboratories and fed in a specific pathogen-free laboratory. All the procedures adhered to guidelines sanctioned by the Animal Ethics Committee of the Hubei Safety Evaluation Center (permit number: 202310005). For all of the experiments, an equivalent mole of isotype (6.6 mg/kg), anti-TGF-β (6.6 mg/kg), anti-PD-L1 (6.6 mg/kg) or YM101 (9 mg/kg) was administered intraperitoneally (i.p.) six times over two weeks [17]. RT was delivered concurrently with the second Ab dose. For the efficacy experiments, the experimental endpoints were defined as either the completion of the treatment protocol or when the tumor volume exceeded 2000 mm^3. The tumor volume was measured using a caliper and was calculated as V = [length × width^2] × 0.5. For the survival analysis, mice were monitored until death or until the median survival time was reached.

4T1 orthotopic tumor model

BALB/c mice were orthotopically implanted with 4T1 cells (1×10^6) in the right mammary fat pad. For the efficacy experiments ($n = 6$/group), upon reaching a mean tumor volume of approximately 150 mm^3, the tumor-bearing mice were randomly allocated into the following six groups: isotype control, YM101, RT (10 Gy), RT combined with anti-PD-L1, RT combined with anti-TGF-β, and RT combined with YM101. Treatment was initiated on Day 0, and the mice were euthanized on Day 12. The tumor volume and mouse weight were recorded on alternate days. For the survival experiments ($n = 9$/group), treatment was initiated at 5 days post inoculation. The survival status of the mice was monitored for 10 weeks.

MC38 and CT26 tumor models

For the efficacy experiments ($n = 6$/group), CT26 (1×10^6) and MC38 (1×10^6) cells were subcutaneously injected into the right groins of BALB/c and C57BL/6 mice. Upon reaching a mean tumor volume of approximately 150 mm^3, the tumor-bearing mice were randomly allocated into the following four groups: isotype control, RT (10 Gy), YM101 and RT combined with YM101. Treatment was initiated on Day 0, and mice were euthanized on either Days 12 or 14. Tumor volume and mouse weight were recorded every one or two days. For the survival experiments ($n = 9$/group), CT26 (1×10^6) cells were subcutaneously injected into the right groins of the BALB/c mice. Treatment was initiated at 7 days post inoculation. The survival status of the mice was monitored for 80 days.

Lung metastasis models

For the CT26 lung metastasis model, mice were intravenously injected via the lateral tail vein with CT26 (2×10^5) cells in 100 μL of PBS. The animals were randomly allocated into the following four groups: isotype control, RT (8 Gy), YM101, and RT combined with YM101. The mice were euthanized at 18 days after tumor cell injection. The lungs were subsequently harvested, and the tumor nodules were counted based on their characteristic appearance. The weights of the lungs were recorded, after which the lungs were fixed for histological evaluation.

The 4T1 spontaneous metastasis model was established via orthotopic implantation of 4T1 (2×10^5) cells into the second mammary fat pads of BALB/c mice, and

the primary tumors were surgically removed at 500–750 mm^3 [37]. After confirming lung metastases in 4 sentinel mice, the remaining mice were randomized into four groups ($n = 6$/group). The mice were euthanized on Day 35, and their lungs were fixed in Bouin's solution, enabling the precise discrimination between tumor nodules and normal lung tissue.

In vivo CD8$^+$ T cell depletion model

For the 4T1 orthotopic model, an anti-CD8 antibody (BioXcell, Cat. BP0061) for the depletion of $CD8^+$ T cells and a rat IgG2b isotype control (BioXcell, Cat. BP0090) as a control were intravenously administered on Day -1 prior to treatment [28]. The efficacy of depletion was confirmed via measurement of the loss of $CD8^+$ T cells in 4T1 tumor tissues, as determined by IHC. When the tumors reached a volume of approximately 150 mm^3, the mice were stratified into three groups ($n = 6$/group for efficacy, $n = 9$/group for survival): CTL (serving as immune-competent controls), Combo (RT + YM101 + rat IgG2b isotype) and Combo + anti-CD8 (RT + YM101 + anti-CD8 depletion).

Flow cytometry analysis and gating strategy

Monocyte-derived dendritic cells (MoDCs) were induced as previously reported [38, 39] and cultured in RPMI-1640 supplemented with 10% FBS, 50 ng/mL murine granulocyte-macrophage colony-stimulating factor (GM-CSF), 50 ng/mL murine IL-4 and 100 U/mL penicillin/streptomycin. The cell morphology was monitored daily using light microscopy. Tumor tissues were collected, digested and filtered as previously reported [17]. Red blood cells were eliminated by ACK lysis buffer (C3702, Beyotime). The samples were incubated with Fixable Viability Stain 700 (564997, BD Biosciences) to exclude dead cells and purified human Fc block (564765, BD Biosciences) or anti-mouse CD16/CD32 antibody (553141, BD Biosciences). Surface marker staining was performed with fluorochrome-conjugated antibodies. Intracellular staining was performed by a Transcription Factor Buffer Set (562574, BD Biosciences). Information regarding the antibodies used for flow cytometry is listed in Additional file 1: Table S1.

Flow cytometry was performed on a Beckman CytoFLEX LX flow cytometer (Beckman Coulter). For the MoDCs, the expression levels are reported as the median fluorescence intensity (MFI) of the $CD11c^+$ population. For the tumor samples, calculation of absolute cell number was performed as previously described [40]. The number of cells obtained for each sample was normalized per 100 mg of tissue. Data analysis was conducted using FlowJo software (v10.8.1, BD).

Unstained controls, single-stained controls and fluorescence minus one (FMO) controls were used to establish compensation and gating threshold determination followed standard quality control practices. Standardized gating strategies were consistently applied across all samples in each experiment.

Cytokine and chemokine measurements

The levels of IL-6 and TNF-α were measured by ELISA. The levels of chemokines were measured with multiplex fluorescence-encoded beads (740985, BioLegend) according to the manufacturer's instructions and analyzed using the dedicated software provided by Biolegend.

Immunohistochemistry (IHC)

All tumor and pulmonary tissues were fixed, dehydrated, and embedded in paraffin. The sections were deparaffinized with xylene and rehydrated through a graded alcohol series. Antigen retrieval was conducted by immersing the sections in citrate buffer (pH 6) via a microwave.

For the 4T1 model, tumor tissue sections were stained with anti-α-SMA (1:800, 192458, CST), anti-collagen I (1:500, ab270993, Abcam) and anti-CD8a (1:200, ab237723, Abcam) antibodies. For all immunostaining analyses, regions of interest (ROIs) were independently delineated by two pathologists. For tumor tissues, 15 non-overlapping fields were randomly selected. The staining intensity was quantitatively analyzed using ImageJ software (v1.53). Standardized threshold criteria were applied across all image evaluations. The number of $CD8^+$ cells in multiple randomly selected microscopic fields was determined via ImageJ software.

Multiplexed Immunofluorescence (IF) staining

Primary antibodies against CD8 (1:4000, ab209775, Abcam), CD4 (1:4000, ab183685, Abcam), FOXP3 (1:4000, 12653, CST), CD11c (1:400, ab52632, Abcam) and CD86 (1:400, 19589, CST) were used. After primary antibody incubation, the sections were incubated with goat anti-rabbit IgG H&L (HRP) (1:4000, ab205718, Abcam) as the secondary antibody. Tyramide signal amplification (TSA) was then performed by iFluor 488 tyramide (1:300, 11060, AAT Bioquest) for CD4 and CD86, iFluor 555 tyramide (1:600, 11065, AAT Bioquest) for FOXP3, and iFluor 647 tyramide (1:400, 11066, AAT Bioquest) for CD8 and CD11c. After the final wash, the nuclei were counterstained with DAPI (C0060, Solarbio).

T-cell infiltration depth was quantified using the mean nearest distance method, as previously described [13]. Briefly, the distance of $CD4^+$ or $CD8^+$ T cells from the tumor margin was measured and scaled relative to the distance from the tumor margin to its center. The CD8/Treg ratio was calculated by dividing the number of $CD8^+$ single-positive cells by the number of $CD4^+FOXP3^+$ double-positive cells in the same area. DC maturation was

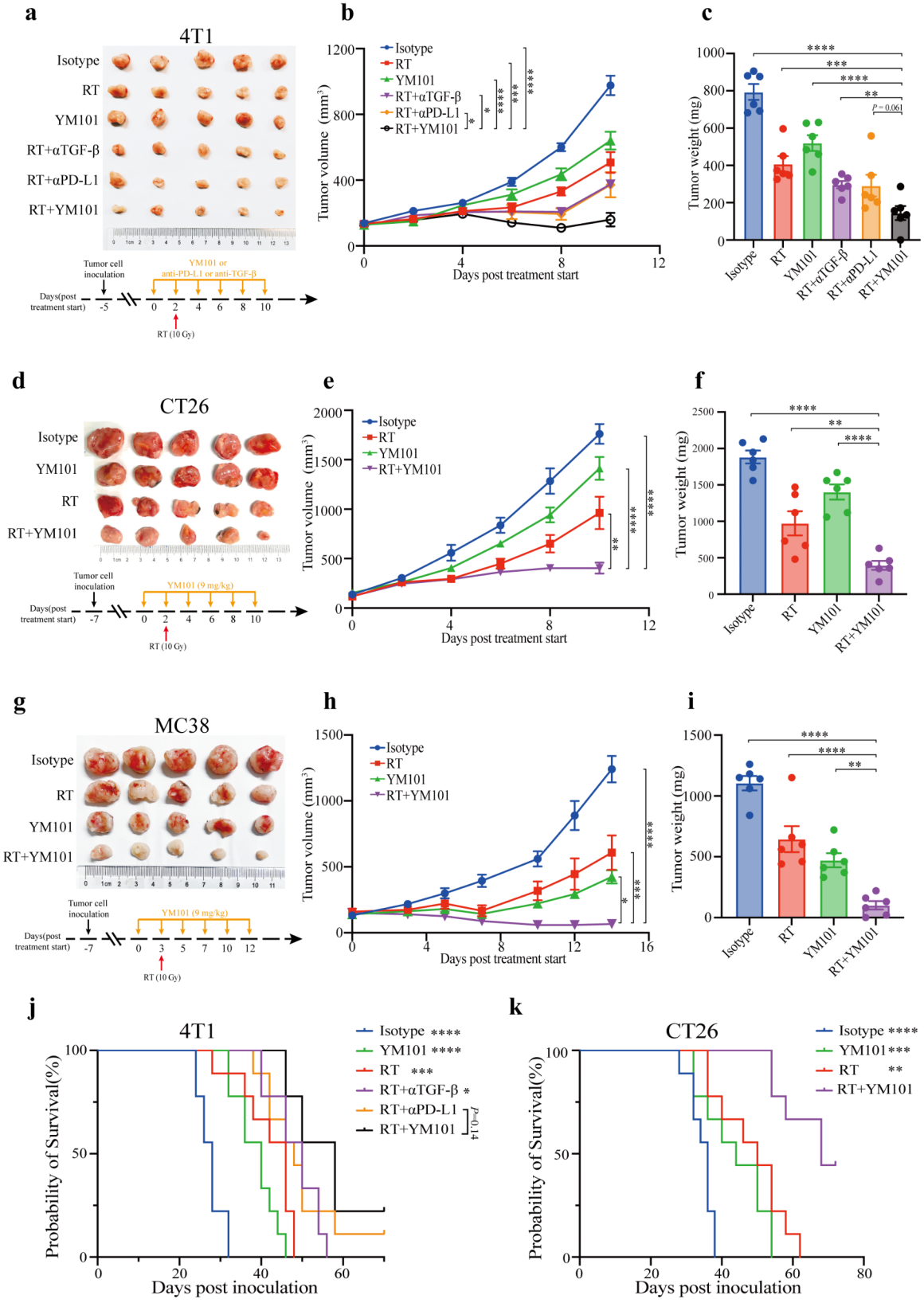

Fig. 1 (See legend on next page.)

(See figure on previous page.)

Fig. 1 RT plus YM101 potentiates tumor suppression across multiple murine models. (**a**-**c**) 4T1 tumor model. (**a**) The representative tumors photograph and schematic of treatment schedules. (**b**) Tumor volume expressed as the mean ± SEM. Data are from three independent experiments with 6–9 mice per group in each experiment. (**c**) Tumor weights on day 12 ($n = 6$ per group). (**d-f**) CT26 tumor model. (**d**) The representative tumors photograph and schematic of treatment schedules. (**e**) Tumor volume expressed as the mean ± SEM. Data are from two independent experiments with 6–9 mice per group in each experiment. (**f**) Tumor weights on day 12 ($n = 6$ per group). (**g-i**) MC38 tumor model. (**g**) The representative tumors photograph and schematic of treatment schedules. (**h**) Tumor volume expressed as the mean ± SEM. (**i**) Tumor weights on day 14 ($n = 6$ per group). (**j-k**) Survival analysis (via Kaplan-Meier) in 4T1 and CT26 tumor-bearing mice were presented ($n = 9$ per group). The *P* values were calculated by one-way ANOVA followed by Dunnett's multiple comparisons test. $^{*}P < 0.05$; $^{**}P < 0.01$; $^{***}P < 0.001$ and $^{****}P < 0.0001$ denote the significant difference relative to RT plus YM101 group when not marked with lines

assessed by quantifying the colocalization of CD11c and CD86 signals.

RIPF murine model and hydroxyproline determination

In the RIPF murine model, C57BL/6 mice received a single dose of 20 Gy to the thorax. The mice in the non-RT group were not irradiated. At 14- or 22- weeks post-RT, the mice were treated with antibodies. The experiments were terminated at 4- or 6- months post-RT. The right lungs were harvested for histological examination, whereas the left lungs were flash-frozen for subsequent biochemical assays. The right pulmonary sections were stained with H&E and Masson's trichrome to assess tissue morphology and fibrosis. Two independent pathologists, blinded to the experimental groups, performed the modified Ashcroft score (scale 0–8) [41]. Five random microscopic fields were examined, with deliberate avoidance of areas adjacent to large airways to prevent bias. The mean score from all fields was calculated to determine the overall fibrosis severity.

Fibrosis was assessed using a colorimetric assay to measure hydroxyproline (HYP) content. Briefly, the left lung tissues were hydrolyzed (95 °C, 20 min), adjusted for pH (6.0–6.8), and processed using a colorimetric HYP assay kit (A030-2-1, Nanjing Jiancheng Bioengineering Institute). The absorbance was measured at 550 nm, and the results are expressed as μg HYP per mg of wet lung tissue.

Blood collection and safety evaluation

After the treatment was terminated, blood samples were collected via retro-orbital puncture. Briefly, blood was collected in EDTA-coated 1.5 mL centrifuge tubes and immediately mixed via gentle shaking. After collection, hemostasis was achieved using sterile cotton balls. Serum was isolated from whole blood via centrifugation under refrigerated conditions. The plasma was then collected for subsequent testing. The plasma samples were analyzed using an AU680 Clinical Chemistry Analyzer (Beckman Coulter) for the detection of alanine aminotransferase (ALT), aspartate aminotransferase (AST), blood urea nitrogen (BUN), creatinine (CRE), and creatine kinase (CK) levels. Moreover, major organs were harvested and stained with H&E for histopathological evaluation.

RNA-sequencing (RNA-seq)

Total RNA was extracted from the 4T1 tumor tissues, and quality was assessed using the RNA Nano 6000 Assay Kit on a Bioanalyzer 2100 system (Agilent Technologies). Sequencing was performed on an Illumina HiSeq 4000 system. The raw reads were processed using fastp software to remove adapters and low-quality sequences. The *Mus musculus* GRCm38 genome was used as a reference. Differential expression analysis was conducted using DESeq2 (v1.26.0). Genes with|log2-fold change| ≥ 1.5 and an adjusted *P*-value < 0.05 were classified as being differentially expressed. Gene Ontology (GO) analyses were performed using the clusterProfiler R package (v3.8.1) [42].

Immune signatures were developed using publicly available datasets [19]. Immune signatures were scored using scaled gene expression and compared using the ROAST algorithm [43].

Statistical analyses

Statistical evaluations were conducted using R studio and GraphPad Prism (v10.2.0). All results are expressed as the mean ± standard error of the mean (SEM). Comparisons between two groups were analyzed using Student's *t* test (unless otherwise explicitly stated). For multiple group comparisons, one-way ANOVA followed by Tukey's or Dunnett's multiple comparisons test was applied. Survival curves were analyzed via Kaplan-Meier estimation, with statistical comparisons performed using log-rank analyses. Statistical significance was denoted as $^{*}P < 0.05$, $^{**}P < 0.01$, $^{***}P < 0.001$ and $^{****}P < 0.0001$.

Results

RT plus YM101 enhances tumor suppression in multiple murine tumor models

Previous studies have suggested that either anti-PD-L1 or TGF-β blockade could synergistically enhance the antitumor effect of RT in 4T1 breast cancer model, which is known for its limited immune cell infiltration and relative resistance to ICIs [44]. Given the intricate nature of the TME and the complex interaction between TGF-β and PD-L1 in immune evasion, we evaluated the efficacy of RT plus YM101 against single-pathway interventions in 4T1 tumor model (Fig. 1a-c). Notably, the combination of RT and YM101 resulted in superior tumor growth

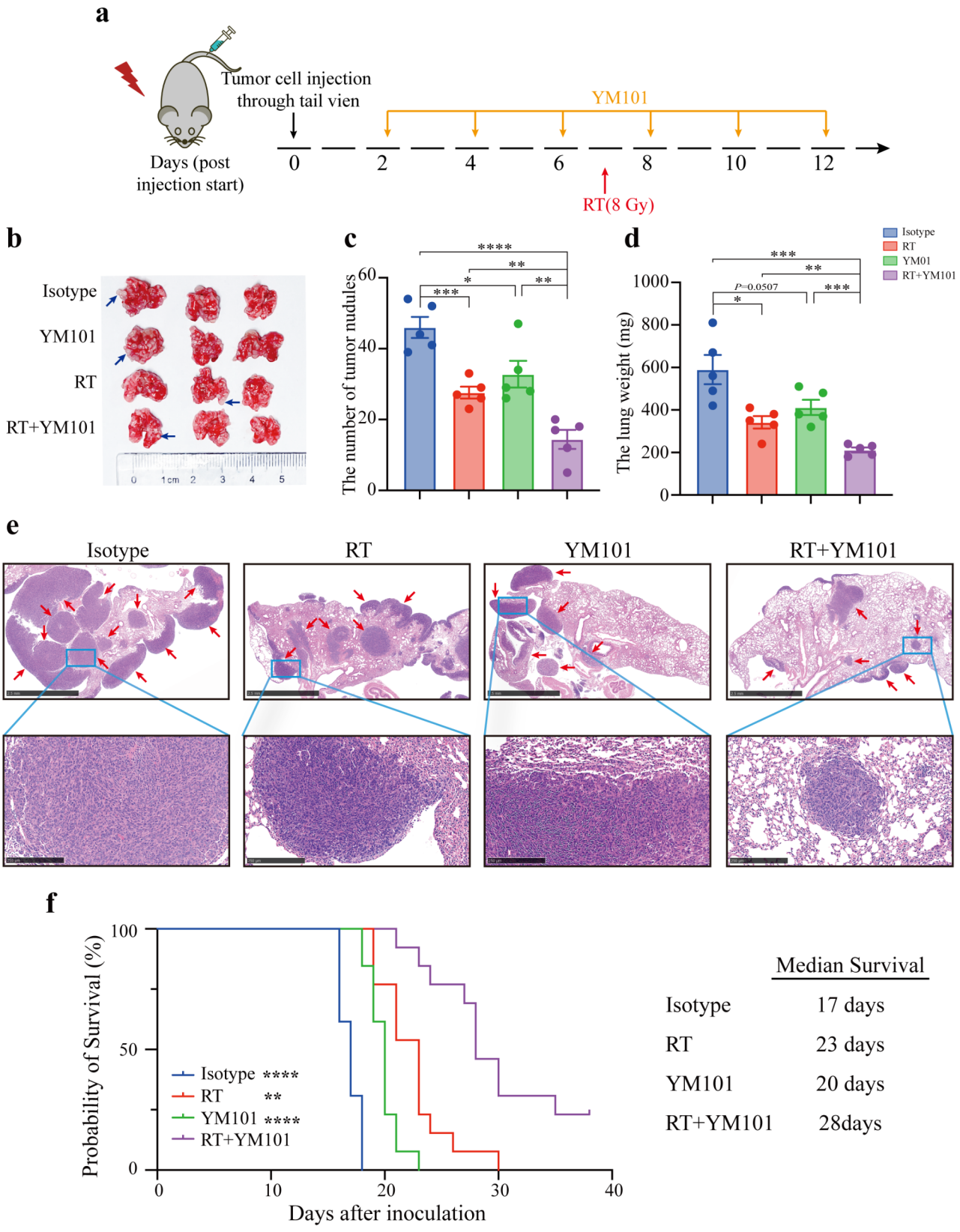

Fig. 2 (See legend on next page.)

(See figure on previous page.)

Fig. 2 RT plus YM101 inhibits incidence of pulmonary metastases. (**a**) Schematic diagrams of treatment for CT26 metastasis model. BALB/c mice were injected with CT26 cell suspension (2×10^5 cells /100 μL) through the tail vein and were randomly separated into four groups: isotype control (i.p., 6.6 mg/kg), RT (8 Gy), YM101 (i.p., 9 mg/kg) and RT combined with YM101 (i.p., 9 mg/kg). (**b**) The representative photographs of metastasized lungs. Blue arrows point to metastatic nodules. (**c**) Quantification of metastatic pulmonary nodules across experimental cohorts on day 18. Data from individual mice and mean ± SEM were shown ($n = 5$ per group). (**d**) The weight of tumor-bearing pulmonary for each group. The *P* values were determined by Student's *t*-test. (**e**) Representative histological images of pulmonary sections stained with H&E showing tumor burden variation within each treatment group. Red arrows point to metastatic nodules. Scale bars represent 2.5 mm and 250 μm, respectively. (**f**) Kaplan-Meier survival analysis of CT26 mice treated with RT or YM101 monotherapy or combined therapy ($n = 9$ per group). Statistical significance determined by log-rank test. *$P < 0.05$; **$P < 0.01$; ***$P < 0.001$ and ****$P < 0.0001$ denote the significant difference relative to RT plus YM101 group when not marked with lines

inhibition and a greater reduction in tumor burden than the use of either RT or YM101 alone. Moreover, RT plus YM101 exhibited enhanced antitumor activity relative to RT plus αTGF-β ($P = 0.0318$), and showed a trend toward improvement compared with RT plus αPD-L1 ($P = 0.061$). To further elucidate the breadth of the efficacy of this combination therapy, we extended our investigation to colorectal cancer (CRC) models using two syngeneic murine models (CT26 and MC38), which exhibit varying degrees of resistance to RT and ICIs. Consistently, RT plus YM101 demonstrated the most potent antitumor activity in both models (Fig. 1d-i).

Long-term survival experiments in both 4T1 and CT26 models revealed significantly improved survival with RT plus YM101 compared with monotherapies (Fig. 1j, k). Furthermore, in the 4T1 model, RT plus YM101 significantly improved survival compared with RT plus αTGF-β ($P = 0.02$), while showing a trend towards significance compared with RT plus αPD-L1 ($P = 0.14$).

The safety assessment of the combination therapy revealed that all the serum biochemical markers (ALT, AST, BUN, CRE, and CK) remained within normal ranges (Additional file 1: Fig. S1a-e) and that there were no histological abnormalities observed in major organs (Additional file 1: Fig. S1f). We also observed stable body weights throughout the treatment (Additional file 1: Fig. S2). These findings demonstrate that RT plus YM101 not only provides superior antitumor efficacy but also maintains a favorable safety profile without systemic toxicity.

RT plus YM101 inhibits the incidence of pulmonary metastases

Pulmonary metastasis represents a major cause of cancer-related mortality, with the lung being a common site for metastatic spread from various primary tumors [45–47]. This scenario is particularly evident in CRC patients, wherein the development of lung metastases is correlated with notably poor clinical outcomes [48]. To evaluate the therapeutic potential of RT plus YM101 in metastatic disease, we established two complementary models: a CT26 experimental metastasis model and a 4T1 spontaneous metastasis model.

In the CT26 metastasis model, tumor cells were intravenously administered to simulate hematogenous spread of cancer. Treatment was initiated on Day 2, followed by targeted lung irradiation being performed using a linear accelerator on Day 7, thereby closely mimicking the clinical RT protocol (Fig. 2a). Analysis of lung tissues on Day 18 revealed that, compared with either monotherapy, RT plus YM101 significantly reduced both the number of visible metastatic nodules and lung weight (Fig. 2b-d). H&E staining further confirmed the substantial reduction in metastatic burden with combination therapy (Fig. 2e). Importantly, RT plus YM101 extended the median survival to 28 days, compared with 20 days with YM101 alone and 23 days with RT alone (Fig. 2f).

To further validate these findings, we employed a 4T1 spontaneous metastasis model, which closely mirrors the metastatic pattern of human breast cancer [49]. Consistent with our CT26 findings, RT plus YM101 markedly reduced pulmonary metastases compared with either monotherapy (Additional file 1: Fig. S3). Collectively, these findings provide compelling evidence that RT plus YM101 effectively inhibits the colonization and progression of pulmonary metastases in vivo.

RT-induced DC maturation and its synergy with YM101 in vivo

Previous studies have observed enhanced DC maturation when cocultured with RT-treated tumor cells [50], thereby suggesting a role for RT in enhancing DC function. However, the the direct effects of RT on DC maturation and function remain poorly understood. To elucidate the influence of RT on DCs, we utilized an in vitro system using monocyte-derived DCs (MoDCs) [51]. After 6 days of culture with GM-CSF and IL-4, the cells exhibited characteristics of immature DCs (imDCs) (Additional file 1: Fig. S4). We subsequently subjected imDCs to a radiation dose gradient to investigate the impact on DC maturation. Flow cytometric analysis revealed that RT, up to 10 Gy, significantly increased the expression of the DC maturation markers CD86, CD80 and CD40 in a dose-dependent manner, wherea higher doses exerted inhibitory effects (Fig. 3a-c). Moreover, across all the tested doses, RT increased the expression of major histocompatibility complex (MHC)-II molecules (HLA-DRs) on DCs, indicating a broad effect on antigen presentation capacity (Additional file 1: Fig. S5a). Importantly, cell viability analysis revealed that the majority of the DCs remained viable after exposure (Additional file 1: Fig.

S5b). In conjunction with increased levels of costimulatory molecules, PD-L1 induced PD-L1 upregulation on DCs after RT (Additional file 1: Fig. S6a, b). Similarly, RT enhanced PD-L1 expression in multiple tumor cell lines, including 4T1, CT26, and MC38 cells (Additional file 1: Fig. S6c-e), and increased intratumoral PD-L1 expression as demonstrated via IHC analysis (Additional file 1: Fig. S6f).

Recent studies have emphasized the importance of cGAS-STING signaling in RT-mediated antitumor immune responses [52, 53]. We further examined the production of cytokines linked to this pathway, with a focus on IL-6 and TNF-α [54, 55]. Our data demonstrated that RT induced the dose-dependent secretion of TNF-α and sustained the elevation of IL-6 (Fig. 3d, e). At 10 Gy, RT significantly increased the levels of multiple proinflammatory chemokines, including CCL3, CCL4, CCL5, CXCL1, CXCL5, CXCL9, and CXCL10, thereby suggesting a broader impact on the inflammatory milieu (Fig. 3f).

To further investigate the impact of RT on DC maturation in the TME, we performed comprehensive flow cytometry (Additional file 1: Fig. S7a) and IF analyses. In the 4T1 model, RT plus YM101 significantly enhanced the presence of intratumoral DCs and activated DCs (Fig. 3g-i and Additional file 1: Fig. S7b). Consistent with these findings, in the CT26 model, RT plus YM101 significantly increased the density of $CD86^+$ DCs compared with either monotherapy (Fig. 3j, k). Moreover, RT plus YM101 significantly increased the density of $F4/80^+$ cells (Additional file 1: Fig. S7c), which aligns with the results of previous studies showing that either RT alone or RT combined with an immunostimulatory agent (cancer vaccine) increased the percentage of $F4/80^+$ macrophages [56–58].

RT plus YM101 attenuates tissue fibrosis and enhances T cell infiltration

RT has been shown to activate TGF-β signaling, which stimulates cancer-associated fibroblasts (CAFs) and promotes tumor progression, metastasis, and therapy resistance [59–61]. In the 4T1 model, RT significantly increased the expression of α-smooth muscle actin (α-SMA), a typical marker of CAF activation (Fig. 4a, b). Similarly, RT enhanced tumor collagen deposition (Fig. 4c, d). YM101 decreased stromal α-SMA levels and collagen deposition compared with the isotype control, which is consistent with our previous observations in the EMT-6 model [17]. Intriguingly, YM101 reversed both the RT-induced increases in α-SMA expression and collagen deposition, which was likely a result of reduced CAF activity. Collectively, these data suggest that YM101 has the potential to counteract RT-induced CAF activation and the subsequent development of fibrosis.

The activation of CAFs and increased collagen deposition induced by RT theoretically impede T cell infiltration into the tumor core. Given the critical role of $CD8^+$ T cells in RT plus immunotherapy-mediated immune responses, we assessed the infiltration and distribution of immune cells within the TME. Compared with either monotherapy, RT plus YM101 substantially enhanced the density of intratumoral $CD8^+$ TILs in the 4T1 model (Fig. 4e, f). IF analysis further revealed that RT plus YM101 not only increased T cell numbers but also improved T cell penetration into the tumor core (Fig. 4g, h). The CD3 staining in the CT26 model also confirms these findings (Additional file 1: Fig. S7d). The improved T cell infiltration and distribution throughout the tumor mass suggest a potential mechanism by which RT plus YM101 overcomes the immunosuppressive barriers typically associated with RT-induced fibrosis.

RT plus YM101 enhances $CD8^+$T cell activation and remodels TIL composition

TILs in the TME have been consistently associated with prognostic outcomes and treatment responses across various solid tumors [62]. Flow cytometry assays were conducted to characterized TIL changes within the TME (Additional file 1: Fig. S8). Compared with either monotherapy, RT plus YM101 significantly increased the numbers of intratumoral total T cells and $CD8^+$ T cells in the 4T1 tumor model. The combination therapy also enhanced the function of $CD8^+$ T cells, as evidenced by increased early-activated ($CD69^+$) and proliferating ($Ki67^+$) and elevated production of inflammatory cytokines ($TNF\text{-}\alpha^+/IFN\text{-}\gamma^+$) and cytotoxic (granzyme $B^+/IFN\text{-}\gamma^+$) $CD8^+$ T cells (Fig. 5a-h). Compared with isotype control or monotherapy, the combination therapy also enhanced NK cell responses, with increased NK cell infiltration and elevated expression of effector molecules (including TNF-α, IFN-γ, perforin, and granzyme B) being observed (Additional file 1: Fig. S9a-e). Additionally, we observed increased $CD4^+$ T cell recruitment and proliferation, as evidenced by increased CD69 and Ki67 expression (Additional file 1: Fig. S9f-h).

Tregs, characterized by their specific expression of the transcription factor forkhead box P3 (FOXP3), play an essential role in tumor immune evasion [63–65]. Given the importance of the $CD8^+$ T cell to Treg ratio in treatment outcomes [66, 67], multiplex IF analysis was conducted and revealed that, although YM101 alone increased $CD8^+$ T cell infiltration compared with controls, the combination with RT led to an even greater enhancement. Crucially, the $CD8^+$/Treg ratio was significantly elevated in the combination group (Fig. 5i-k). This shift towards a more inflammatory immune landscape aligns with improved therapeutic. Notably, this elevated ratio was primarily driven by the increase in $CD8^+$ T cells

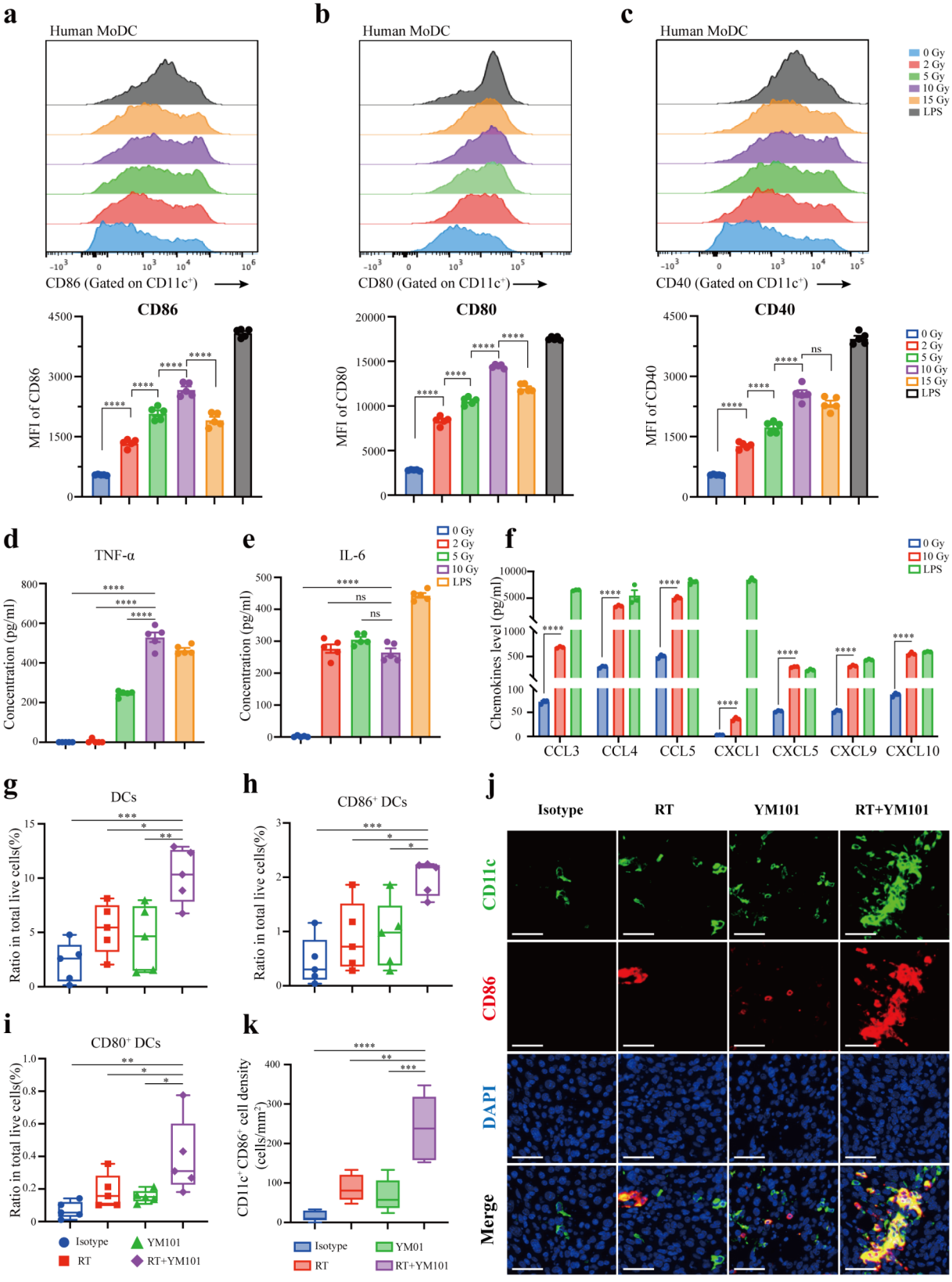

Fig. 3 (See legend on next page.)

(See figure on previous page.)

Fig. 3 RT plus YM101 induced DCs maturation and activation. (**a-c**) $CD14^+$ monocytes were cultured for 6 days with GM-CSF and IL-4. ImDCs were irradiated with 0 Gy, 2 Gy, 5 Gy, 10–15 Gy and cultured for 24 h. ImDCs were stimulated with LPS (1 μg/mL) as a positive control and cultured for 24 h. Representative flow cytometry histograms of CD80, CD86, and CD40 expression on DCs ($n = 5$ independent experiments). (**d-e**) ImDCs were irradiated with 0 Gy, 2 Gy, 5–10 Gy and cultured for 24 h. ImDCs were stimulated with LPS (1 μg/mL) as a positive control and cultured for 24 h. The levels of TNF-α and IL-6 were measured by ELISA ($n = 5$ independent experiments). (**f**) ImDCs were irradiated with 0–10 Gy and cultured for 24 h. ImDCs were stimulated with LPS (1 μg/mL) as a positive control and cultured for 24 h. Chemokines secretion was analyzed by ELISA ($n = 3$ independent experiments). Representative data in a-f were repeated at least three times with similar results. (**g-i**) In the 4T1 model, mice were sacrificed 5 days post RT (for DC maturation analysis) ($n = 5$ mice/group). In the FACS assays, quantification of total DCs (**g**), $CD80^+$ DCs (**h**) and $CD86^+$ DCs (**i**). The *P* values were determined by one-way ANOVA with Dunnett's multiple comparisons test. (**j-k**) Representative IF staining images of CD11c (green) and CD86 (red). Scale bars represent 50 μm. All experiments were repeated 2 or 3 times yielding similar results. $^*P < 0.05$; $^{**}P < 0.01$; $^{***}P < 0.001$; $^{****}P < 0.0001$

rather than a reduction in Treg (Additional file 1: Fig. S9i).

To directly assess the role of $CD8^+$ T cells in mediating therapeutic efficacy, we performed antibody-mediated depletion experiments. Based on the results of the IHC analysis of tumor tissues, we established an effective depletion strategy by an anti-CD8 antibody at 200 μg per mouse (Additional file 1: Fig. S10a, b). Compared with nondepleted controls, $CD8^+$ T cell depletion significantly compromised the antitumor effects of RT plus YM101, resulting in accelerated tumor growth and reduced survival (Fig. 5l-n and Additional file 1: Fig. S10c).

RT plus YM101 reshapes the tumor immune landscape

To elucidate the molecular mechanisms driving the enhanced efficacy of RT and YM101 combination therapy, we performed transcriptomic analysis of 4T1 tumors. The differential gene expression (DEG) map revealed distinct gene expression patterns across the four treatment conditions, with RT plus YM101 demonstrating the most pronounced changes (Fig. 6a). Gene Ontology (GO) enrichment analysis demonstrated that, compared with RT alone, combination therapy significantly upregulated chemokine-mediated signaling pathways and T cell activation (Fig. 6b). Similarly, the comparison of RT plus YM101 to YM101 alone revealed enrichment of pathways related to the IFN-γ response, innate immune responses and MHC protein complex binding (Fig. 6c). RT plus YM101 combined treatment activated immune-related pathways to a greater degree.

Further analysis of immune cell-specific gene signatures revealed that, compared with either monotherapy, RT plus YM101 significantly enhanced the expression of genes associated with T cells, NK cells, the IFN-α response and the IFN-β response (Fig. 6d-g). These transcriptomic findings provide molecular evidence that RT plus YM101 combination therapy effectively remodels the tumor immune microenvironment, corroborating our observed improvements in tumor control and survival outcomes.

YM101 ameliorates radiation-induced pulmonary fibrosis (RIPF)

RIPF represents a critical late-stage complication of thoracic RT and is characterized by excessive collagen deposition and compromised pulmonary function [68]. To elucidate the therapeutic potential of YM101 in mitigating RIPF, we established a murine model with a single dose of 20 Gy thoracic irradiation(Fig. 7a). Pulmonary sections were collected at 4 and 6 months post-RT and stained with H&E for structural features and Masson's trichrome for collagen deposition. To ensure comprehensive and unbiased assessments, the analysis process involved an initial examination of complete pulmonary at low magnification, followed by a more detailed examination of each section under 200× magnification (Additional file 1: Fig. S11).

Histological analysis revealed that irradiated lungs treated with the isotype control or anti-PD-L1 antibody exhibited severe fibrotic changes, characterized by alveolar collapse, interalveolar septal thickening, and dense inflammatory infiltrates. Masson's trichrome staining demonstrated marked collagen accumulation in these groups (Fig. 7b, c). Notably, both the anti-TGF-β and YM101 treatments significantly attenuated these fibrotic changes, whereby these treatments preserved alveolar structure and reduced collagen deposition in the alveolar septa. Quantitative assessment of fibrosis via Ashcroft scoring confirmed these observations (Fig. 7d).

To further validate these observations, we quantified the content of hydroxyproline (HYP), which is the gold standard biochemical marker of pulmonary fibrosis severity [69]. HYP analysis at both 4 and 6 months post-RT revealed a consistent pattern: non-RT group maintained low HYP levels, whereas irradiated mice treated with isotype or anti-PD-L1 antibodies exhibited significantly elevated HYP levels (Fig. 7e, f). Both the anti-TGF-β and YM101 treatments effectively reduced HYP levels, with YM101 demonstrating superior fibrosis mitigation efficacy at 6 months post-RT.

Discussion

Our study demonstrated the therapeutic potential of combining RT with YM101 (a novel bispecific antibody that targets TGF-β and PD-L1) for treating non-inflamed

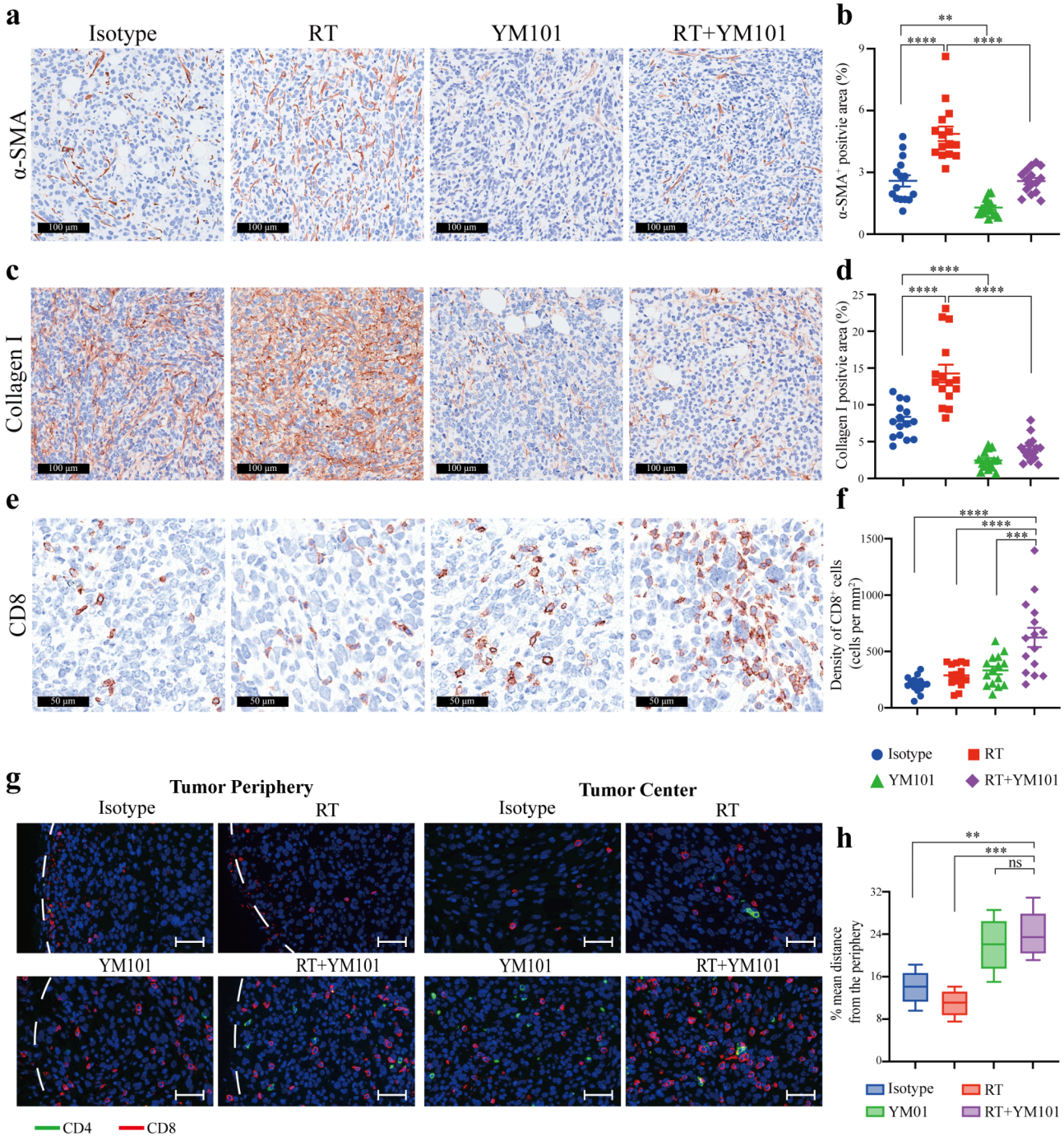

Fig. 4 RT plus YM101 attenuates tissue fibrosis and increases infiltration. (**a-f**) 4T1 tumor-bearing mice received isotype, YM101, RT or combination therapy. Tumor tissues were harvested at day 10 post RT. Representative IHC images and quantifications of tumor sections stained with an anti-α-SMA, anti-collagen I and anti-CD8 antibody. Scale bars represent 50 and 100 μm. Each point on the graphs represents an individual fields ($N = 15$ fields, 5 mice). (**g**) The representative CD4 (green) and CD8 (red) IF staining of tumor periphery and center. Dashed line indicates tumor boundaries. Scale bars represent 50 μm. (**h**) Quantification of infiltration depth of T cells based on IHC. The *P* values were determined using one-way ANOVA followed by Tukey's multiple comparisons test. $P < 0.01$; * $P < 0.001$; **** $P < 0.0001$; ns: not significant

tumors (Fig. 8). Compared with monotherapies, this combination therapy exhibited superior antitumor efficacy across multiple tumor models while simultaneously mitigating RIPF.

Although multiple preclinical studies have revealed stronger antitumor activities of RT combined with ICIs [70], resistance frequently persists, thereby indicating the existence of additional immunosuppressive pathways

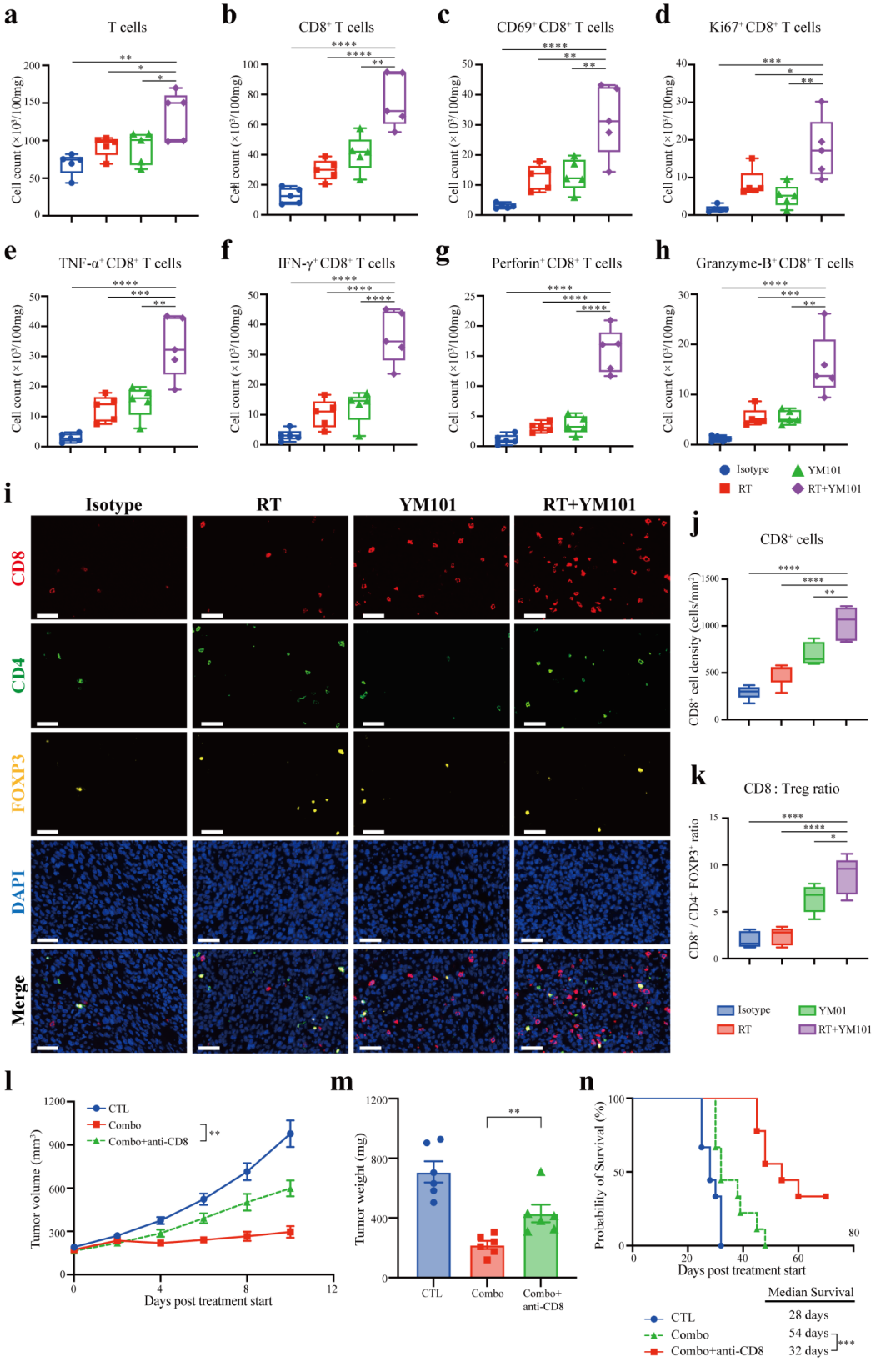

Fig. 5 (See legend on next page.)

(See figure on previous page.)

Fig. 5 RT plus YM101 promoted $CD8^+$ T cell activation in the 4T1 murine model. (**a-h**) Flow cytometry analysis of tumors from BALB/c mice subcutaneously inoculated with 4T1 cells and sacrificed two days after the completion of treatment. Quantification of total T cells (**a**), $CD8^+$ T cells (**b**), activated $CD8^+$ T cells ($CD69^+$) (**c**), $Ki67^+$ $CD8^+$ T cells (**d**), TNF-α^+ $CD8^+$ T cells (**e**), IFN-γ^+ $CD8^+$ T cells (**f**), $Perforin^+$ $CD8^+$ T (**g**) and Granzyme-B^+ $CD8^+$ T cells (**h**). Each point represents an individual mouse ($n = 5$ per group). (**i**) Representative images from CD8 (red), CD4 (green) and FOXP3 (yellow) in CT26 tumors stained by IF. Scale bars represent 50 μm. (**j**) Quantification of $CD8^+$ T cell density (cells/mm^2) in multiplexed IF images of tumor area. (**k**) $CD8^+$ T cell/Treg ratio in tumor area based on multiplexed IF analysis. (**l-n**) Effect of $CD8^+$ T cell depletion on combined therapy in the 4T1 tumor model. (**l**) Tumor volume expressed as the mean ± SEM. Data are from two independent experiments with 6 or 9 mice per group in each experiment. (**m**) Tumor weights on day 12 ($n = 6$ per group). (**n**) Kaplan-Meier plot of survival by treatment group and median survival are presented. The *P* values were determined using a one-way ANOVA followed by Dunnett's multiple comparisons test. *$P < 0.05$; ** $P < 0.01$; *** $P < 0.001$; **** $P < 0.0001$

[67, 71]. The superior antitumor activity observed with RT plus YM101 compared with either monotherapy or RT combined with anti-PD-L1 highlights the importance of the simultaneous targeting of multiple immunosuppressive mechanisms within the TME. This observation is particularly significant in the context of non-inflamed tumors, which represent a major challenge for cancer immunotherapy. These tumors are characteristically resistant to currently used immunotherapies due to a combination of factors, including the lack of tumor antigens, hampered DC maturation, inadequate initiation and stimulation of T cells, and compromised T cell infiltration [72]. Our results align with increasing evidence suggesting that successful cancer immunotherapy requires both the stimulation of innate immunity and increased T cell infiltration and activation within the TME [73, 74].

A key observation in our study was the ability of RT to modulate DC maturation. Although previous research has focused on enhanced DC maturation when cocultured with irradiated tumor cells [50], our study provides direct evidence of the impact of RT on DC activation and proinflammatory cytokine production. Furthermore, we demonstrated that RT directly increases PD-L1 expression on both tumor cells and DCs, providing a strong mechanistic rationale for combining RT with YM101. The upregulation of PD-L1 on DCs is particularly significant, as recent studies have suggested that DC expressed PD-L1 may be more predictive of clinical responses than PD-L1 expression in tumor cells [38, 75]. This observation aligns with emerging evidence highlighting the critical role of DCs in mediating successful antitumor immune responses.

RT-induced DC activation leads to a cascade of downstream immune effects. Mechanistically, via improved antigen cross-presentation, activated DCs effectively sensitized and expanded tumor-specific T cells, as evidenced by increased levels of activation and proliferation markers on $CD8^+$ T cells, as well as elevated production of TNF-α, IFN-γ, perforin and granzyme B, in the flow cytometry. Moreover, the increased ratio of $CD8^+$ T cells to Tregs further shifts the balance in favor of antitumor immunity [76]. The essential role of $CD8^+$ T cells in mediating the therapeutic efficacy of RT plus YM101 combination therapy was conclusively demonstrated via depletion experiments, wherein $CD8^+$ T cell depletion abolished the antitumor effects of combination therapy. Interestingly, we also observed increased numbers of NK cells and $CD4^+$ T cells, which likely resulted from the enriched cytokine milieu created by activated DCs and the reciprocal interactions between different immune cell populations within the TME.

The ability of YM101 to reverse RT-induced CAF activation and collagen deposition represents another crucial mechanism underlying the efficacy of this combination therapy. By targeting TGF-β, YM101 helps to dismantle the physical and functional barrier created by CAFs and their associated extracellular matrix components, potentially facilitating immune effector cell expansion, particularly $CD8^+$ T cells infiltration. Moreover, RNA-seq analysis reveals a comprehensive remodeling of the TME following combination treatment. These synergistic effects provide a strong mechanistic basis for the superior efficacy of combination therapy compared with either monotherapy.

Importantly, our study provides novel insights into the synergistic effects of dual PD-L1 and TGF-β blockade in mitigating RIPF. Although anti-PD-L1 monotherapy had a minimal effect on RIPF, YM101 demonstrated slightly superior efficacy over a longer period compared with anti-TGF-β alone. Recent single-cell sequencing data have revealed that in fibrotic lungs, TGF-β expression is predominantly localized to specific PD-L1-expressing cell populations, particularly in specific endothelial cell subsets and M2/lipofibroblast-like cells [28], which may provide context for these observations. The ability of YM101 to attenuate RIPF while enhancing antitumor efficacy potentially broadens the therapeutic window for RT in cancer treatment.

However, several limitations of our study require further investigation, particularly the optimal timing and sequencing of RT and YM101 administration, as well as the RT dosing and fractionation schedules, as these parameters may significantly impact therapeutic outcomes [77–79]. Additionally, the long-term effects and potential toxicities of this combination approach warrant careful investigation [31, 32]. Although our safety evaluation revealed no overt systemic toxicity, more comprehensive studies are needed to comprehensively assess the risk-benefit ratio of RT combined with YM101.

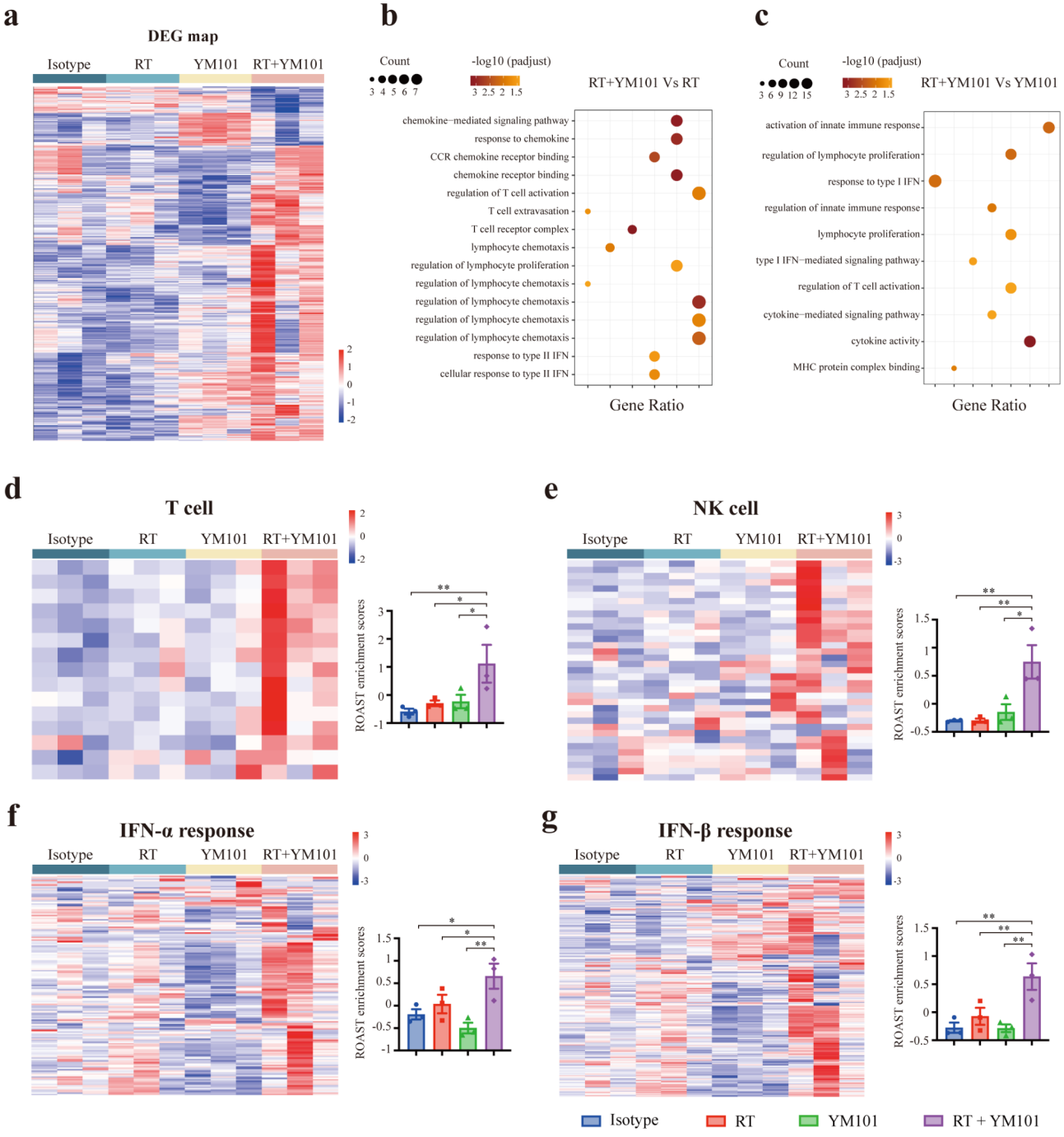

Fig. 6 RT plus YM101 reshapes the tumor immune landscape in the 4T1 model. (**a**) Heatmap visualization of differentially expressed genes (DEGs) across different treatment groups. DEGs were identified using the following criteria:|log2 fold change| ≥ 1.5 and adjusted *P*-value < 0.05. Gene lists and statistical information are provided in Additional file 1: Table S2. (**b-c**) GO enrichment analysis between RT plus YM101 and monotherapy groups (RT + YM101 Vs. YM101 and RT + YM101 Vs. RT, respectively). Immune-related GO enrichment results are detailed in Additional file 1: Table S3. (**d-g**) Analysis of immune signature enrichment using ROAST algorithm. The heatmaps depicted the normalized expression level of genes sets. The plots show the distribution of ROAST enrichment scores for gene sets across different experimental groups. For each signature, scores were calculated using the ROAST mean statistic with genes listed in Additional file 1: Table S4. **P* < 0.05; ** *P* < 0.01

The translational potential of this approach is supported by the ongoing clinical development of Y101D, the humanized version of YM101. A phase I clinical trial (NCT05028556) has already demonstrated the safety of Y101D, paving the way for phase Ib/II combination therapy studies. Future studies should address the identified limitations through larger-scale investigations, diverse tumor models, and detailed mechanistic analyses.

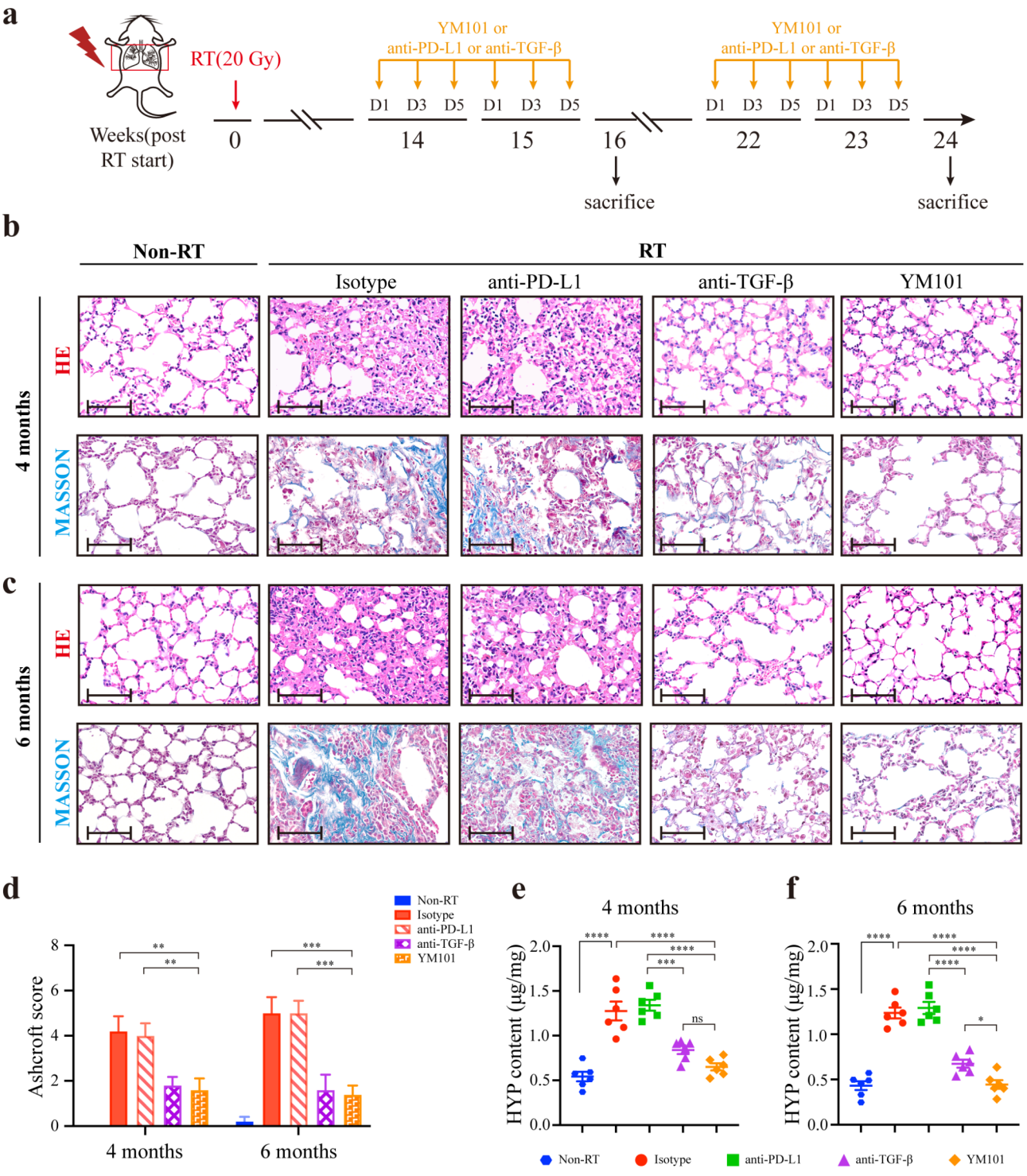

Fig. 7 YM101 ameliorates radiation-induced pulmonary fibrosis (RIPF). (**a**) Schematic diagrams for intervention of RILF model. C57BL/6 mice ($n=12$) underwent thoracic irradiation (a single dose of 20 Gy), and after 4 months and 6 months, were treated with isotype, anti-TGF-β, anti-PD-L1, or YM101. 6 mice sacrificed 16 months post RT, and 6 mice sacrificed 24 months post RT. (**b-c**) Representative images of H&E (upper panel) and Masson's trichrome staining (lower panel) of right lung sections from mice surviving 4- (**b**) and 6- (**c**) months post RT. Scale bars represent 100 μm. Blue stain in lower panel indicates collagen deposition. (**d**) Ashcroft score was used to determine the pulmonary fibrosis degree. (**e-f**) The hydroxyproline (HYP) content (μg of HYP per mg of wet lung tissue) in left lung homogenates at 4- and 6-months post-RT ($n=6$ per group). The data are expressed as mean ± SEM. $^{**}P<0.01$, $^{***}P<0.001$; $^{****}P<0.0001$

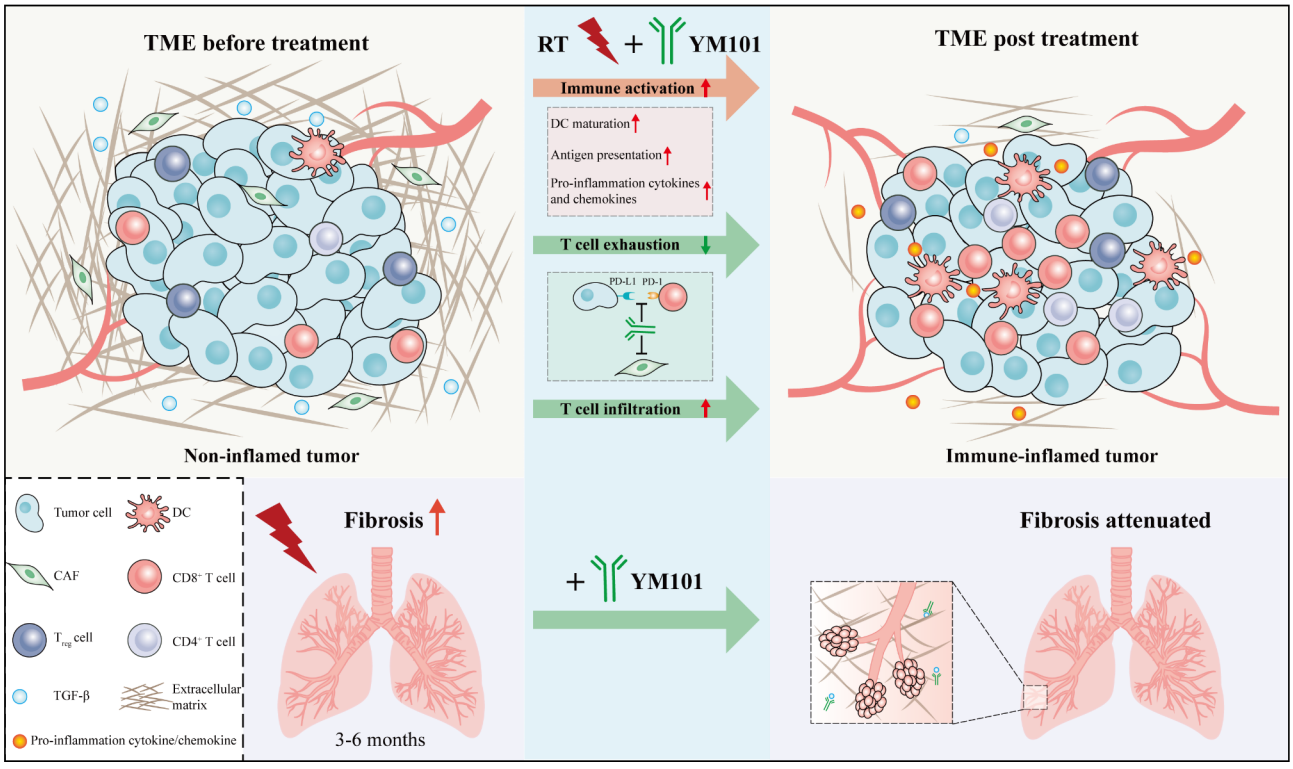

Fig. 8 Mechanism of RT and YM101 combined therapy. Upper panels illustrate that schematic representation of the tumor microenvironment (TME) before and after treatment with RT and YM101. Combined RT and YM101 treatment induce multiple effects, including immune activation (increased DC maturation and pro-inflammatory cytokine/chemokine production), reduced T cell exhaustion, and enhanced T cell infiltration. Lower panels illustrate the impact of YM101 on radiation-induced pulmonary fibrosis (RIPF), demonstrating attenuated ECM deposition and fibrosis. The ability to attenuate RIPF while enhancing antitumor efficacy potentially broaden the therapeutic window for RT in the cancer treatment

Careful clinical trial design and comprehensive patient monitoring will be essential for successful translation of these preclinical findings.

Conclusion

Our study provides compelling evidence for the therapeutic efficacy of combining RT with YM101 (a bispecific antibody that targets TGF-β and PD-L1) in murine breast cancer and colorectal cancer models. This combination therapy demonstrated superior antitumor effects compared with either monotherapy. Mechanistically, our findings reveal that this combination therapy comprehensively orchestrates the TME remodeling by promoting DC maturation, reversing CAF activation, and facilitating robust $CD8^+$ T cell infiltration and activation. In particular, YM101 not only enhances the antitumor efficacy of RT but also mitigates RILF, addressing a critical clinical challenge of RT. These findings establish a robust preclinical foundation and provide a compelling rationale for future clinical investigations of RT combined with YM101, particularly in patients with non-inflamed and stroma-rich tumors resistant to current immunotherapies.

Abbreviations

ICIs	Immune checkpoint inhibitors
PD-L1	Programmed cell death-ligand 1
RT	Radiotherapy
TME	Tumor microenvironment
CAF	Carcinoma-associated fibroblast
TGF-β	Transforming growth factor-beta
Treg	Regulatory T cell
DC	Dendritic cells
TMB	Tumor mutational burden
TILs	Tumor-infiltrating lymphocytes
ICD	Immunogenic cell death
RIPF	Radiation-induced pulmonary fibrosis
MoDCs	Monocyte-derived DCs
GM-CSF	Granulocyte–macrophage colony-stimulating factor
ImDCs	Immature MoDCs
MHC	Major histocompatibility complex
FOXP3	Forkhead box P3
FBS	Fetal bovine serum
ELISA	Enzyme-linked immunosorbent assay
α-SMA	α-smooth muscle actin
MFI	Mean fluorescence intensity
ROI	Regions of interest
HYP	Hydroxyproline
DEG	Differently expressed gene
ALT	Alanine aminotransferase
AST	Aspartate aminotransferase
BUN	Blood urea nitrogen
CRE	Creatinine
CK	Creatine kinase
GO	Gene Ontology
SEM	Standard error of the mean

CRC Colorectal cancer

Supplementary Information

The online version contains supplementary material available at https://doi.org/10.1186/s13045-025-01678-2.

Supplementary Material 1

Acknowledgements
We would like to thank Dr. Chen Yaobing in Pathology Analysis Department, Hubei Biossci Biotechnology, Inc. for contributions to the histopathological analysis.

Author contributions
YW conducted major experiments and drafted the manuscript. YY, YG, MN and BZ participated in data collection and presentention, JZ, PZ and QC helped experimental design and data analysis. MY and QM participated in the analysis and interpretation of data. KW supervised this work.

Funding
This work was supported by the National Natural Science Foundation of China (No. 82073370, 82272794).

Data availability
The dataset generated during the current study is available from the corresponding author on reasonable request. All raw RNA-seq data are publicly available in National Center for Biotechnology Information Sequence Read Archive under accession number PRJNA1213013.

Declarations

Ethics approval and consent to participate
The animal operations in this study were evaluated and approved by the Animal Ethics Committee of Hubei Safety Evaluation Center (permit number: 202310005). All procedures adhered to protocols approved.

Consent for publication
Not applicable.

Competing interests
JZ and PZ were employees of Wuhan YZY Biopharma Co., Ltd.

Author details
[1]Department of Oncology, Tongji Hospital of Tongji Medical College, Huazhong University of Science and Technology, 1095 Jiefang Avenue, Wuhan 430030, China
[2]Cancer Center, Tongji Shanxi Hospital, Shanxi Bethune Hospital, Shanxi Academy of Medical Science, Third Hospital of Shanxi Medical University, Taiyuan 030032, China
[3]Wuhan YZY Biopharma Co., Ltd., Biolake, C2-1, No.666 Gaoxin Road, Wuhan 430075, China
[4]Department of Breast Surgery, Zhejiang University School of Medicine First Affiliated Hospital, Hangzhou 310000, China
[5]Cancer Center, Tongji Hospital of Tongji Medical College, Huazhong University of Science and Technology, Wuhan 430032, China

Received: 28 August 2024 / Accepted: 17 February 2025
Published online: 05 March 2025

References

1. Yang K, Halima A, Chan TA. Antigen presentation in cancer - mechanisms and clinical implications for immunotherapy. Nat Rev Clin Oncol. 2023;20(9):604–23.
2. Schmid P, Cortes J, Pusztai L, McArthur H, Kümmel S, Bergh J, Denkert C, Park YH, Hui R, Harbeck N, et al. Pembrolizumab for early Triple-Negative breast Cancer. N Engl J Med. 2020;382(9):810–21.
3. Andre T, Elez E, Van Cutsem E, Jensen LH, Bennouna J, Mendez G, Schenker M, de la Fouchardiere C, Limon ML, Yoshino T, et al. Nivolumab plus ipilimumab in Microsatellite-Instability-High metastatic colorectal Cancer. N Engl J Med. 2024;391(21):2014–26.
4. Guan WL, He Y, Xu RH. Gastric cancer treatment: recent progress and future perspectives. J Hematol Oncol. 2023;16(1):57.
5. Haslam A, Prasad V. Estimation of the percentage of US patients with Cancer who are eligible for and respond to checkpoint inhibitor immunotherapy drugs. JAMA Netw Open. 2019;2(5):e192535.
6. Mok TSK, Wu YL, Kudaba I, Kowalski DM, Cho BC, Turna HZ, Castro G Jr., Srimuninnimit V, Laktionov KK, Bondarenko I, et al. Pembrolizumab versus chemotherapy for previously untreated, PD-L1-expressing, locally advanced or metastatic non-small-cell lung cancer (KEYNOTE-042): a randomised, open-label, controlled, phase 3 trial. Lancet. 2019;393(10183):1819–30.
7. Ma W, Xue R, Zhu Z, Farrukh H, Song W, Li T, Zheng L, Pan CX. Increasing cure rates of solid tumors by immune checkpoint inhibitors. Exp Hematol Oncol. 2023;12(1):10.
8. Xu L, Zou C, Zhang S, Chu TSM, Zhang Y, Chen W, Zhao C, Yang L, Xu Z, Dong S, et al. Reshaping the systemic tumor immune environment (STIE) and tumor immune microenvironment (TIME) to enhance immunotherapy efficacy in solid tumors. J Hematol Oncol. 2022;15(1):87.
9. Jia Q, Wang A, Yuan Y, Zhu B, Long H. Heterogeneity of the tumor immune microenvironment and its clinical relevance. Exp Hematol Oncol. 2022;11(1):24.
10. Chen DS, Mellman I. Elements of cancer immunity and the cancer–immune set point. Nature. 2017;541(7637):321–30.
11. Zheng S, Wang W, Shen L, Yao Y, Xia W, Ni C. Tumor battlefield within inflamed, excluded or desert immune phenotypes: the mechanisms and strategies. Exp Hematol Oncol. 2024;13(1):80.
12. Hegde PS, Chen DS. Top 10 challenges in Cancer immunotherapy. Immunity. 2020;52(1):17–35.
13. Mariathasan S, Turley SJ, Nickles D, Castiglioni A, Yuen K, Wang Y, Kadel EE III, Koeppen H, Astarita JL, Cubas R, et al. TGFβ attenuates tumour response to PD-L1 Blockade by contributing to exclusion of T cells. Nature. 2018;554(7693):544–8.
14. Tauriello DVF, Sancho E, Batlle E. Overcoming TGFβ-mediated immune evasion in cancer. Nat Rev Cancer. 2022;22(1):25–44.
15. Massagué J, Sheppard D. TGF-β signaling in health and disease. Cell. 2023;186(19):4007–37.
16. Richardson L, Wilcockson SG, Guglielmi L, Hill CS. Context-dependent TGFβ family signalling in cell fate regulation. Nat Rev Mol Cell Biol. 2023;24(12):876–94.
17. Yi M, Zhang J, Li A, Niu M, Yan Y, Jiao Y, Luo S, Zhou P, Wu K. The construction, expression, and enhanced anti-tumor activity of YM101: a bispecific antibody simultaneously targeting TGF-β and PD-L1. J Hematol Oncol. 2021;14(1):27.
18. Cheng B, Ding K, Chen P, Ji J, Luo T, Guo X, Qiu W, Ma C, Meng X, Wang J, et al. Anti-PD-L1/TGF-βR fusion protein (SHR-1701) overcomes disrupted lymphocyte recovery-induced resistance to PD-1/PD-L1 inhibitors in lung cancer. Cancer Commun (Lond). 2022;42(1):17–36.
19. Lan Y, Zhang D, Xu C, Hance KW, Marelli B, Qi J, Yu H, Qin G, Sircar A, Hernández VM et al. Enhanced preclinical antitumor activity of M7824, a bifunctional fusion protein simultaneously targeting PD-L1 and TGF-β. Sci Transl Med. 2018;10(424).
20. Reardon DA, Brandes AA, Omuro A, Mulholland P, Lim M, Wick A, Baehring J, Ahluwalia MS, Roth P, Bähr O, et al. Effect of nivolumab vs bevacizumab in patients with recurrent glioblastoma: the checkmate 143 phase 3 randomized clinical trial. JAMA Oncol. 2020;6(7):1003–10.
21. Galon J, Bruni D. Approaches to treat immune hot, altered and cold tumours with combination immunotherapies. Nat Rev Drug Discov. 2019;18(3):197–218.
22. Demaria O, Cornen S, Daëron M, Morel Y, Medzhitov R, Vivier E. Harnessing innate immunity in cancer therapy. Nature. 2019;574(7776):45–56.
23. Yi M, Li T, Niu M, Mei Q, Zhao B, Chu Q, Dai Z, Wu K. Exploiting innate immunity for cancer immunotherapy. Mol Cancer. 2023;22(1):187.
24. Shaverdian N, Lisberg AE, Bornazyan K, Veruttipong D, Goldman JW, Formenti SC, Garon EB, Lee P. Previous radiotherapy and the clinical activity and toxicity of pembrolizumab in the treatment of non-small-cell lung cancer: a secondary analysis of the KEYNOTE-001 phase 1 trial. Lancet Oncol. 2017;18(7):895–903.
25. Antonia SJ, Villegas A, Daniel D, Vicente D, Murakami S, Hui R, Kurata T, Chiappori A, Lee KH, de Wit M, et al. Overall survival with durvalumab after chemoradiotherapy in stage III NSCLC. N Engl J Med. 2018;379(24):2342–50.

26. Galluzzi L, Aryankalayil MJ, Coleman CN, Formenti SC. Emerging evidence for adapting radiotherapy to immunotherapy. Nat Rev Clin Oncol. 2023;20(8):543–57.
27. Grassberger C, Ellsworth SG, Wilks MQ, Keane FK, Loeffler JS. Assessing the interactions between radiotherapy and antitumour immunity. Nat Rev Clin Oncol. 2019;16(12):729–45.
28. Lan Y, Moustafa M, Knoll M, Xu C, Furkel J, Lazorchak A, Yeung TL, Hasheminasab SM, Jenkins MH, Meister S, et al. Simultaneous targeting of TGF-β/PD-L1 synergizes with radiotherapy by reprogramming the tumor microenvironment to overcome immune evasion. Cancer Cell. 2021;39(10):1388–e14031310.
29. Barker HE, Paget JT, Khan AA, Harrington KJ. The tumour microenvironment after radiotherapy: mechanisms of resistance and recurrence. Nat Rev Cancer. 2015;15(7):409–25.
30. Vanpouille-Box C, Diamond JM, Pilones KA, Zavadil J, Babb JS, Formenti SC, Barcellos-Hoff MH, Demaria S. TGFβ is a master regulator of radiation Therapy-Induced antitumor immunity. Cancer Res. 2015;75(11):2232–42.
31. Jabbour SK, Lee KH, Frost N, Breder V, Kowalski DM, Pollock T, Levchenko E, Reguart N, Martinez-Marti A, Houghton B, et al. Pembrolizumab plus concurrent chemoradiation therapy in patients with unresectable, locally advanced, stage III Non-Small cell lung cancer: the phase 2 KEYNOTE-799 nonrandomized trial. JAMA Oncol. 2021;7(9):1–9.
32. Wang Y, Zhang T, Huang Y, Li W, Zhao J, Yang Y, Li C, Wang L, Bi N. Real-World safety and efficacy of consolidation durvalumab after chemoradiation therapy for stage III Non-small cell lung cancer: A systematic review and Meta-analysis. Int J Radiat Oncol Biol Phys. 2022;112(5):1154–64.
33. Hanania AN, Mainwaring W, Ghebre YT, Hanania NA, Ludwig M. Radiation-Induced lung injury: assessment and management. Chest. 2019;156(1):150–62.
34. Yi M, Yuan Y, Ma L, Li L, Qin W, Wu B, Zheng B, Liao X, Hu G, Liu B. Inhibition of TGFβ1 activation prevents radiation-induced lung fibrosis. Clin Translational Med. 2024;14(1):e1546.
35. Bian C, Qin WJ, Zhang CY, Zou GL, Zhu YZ, Chen J, Zhao R, Wang YY, Zhe H. Thalidomide (THD) alleviates radiation induced lung fibrosis (RILF) via down-regulation of TGF-β/Smad3 signaling pathway in an Nrf2-dependent manner. Free Radic Biol Med. 2018;129:446–53.
36. Yi M, Wu Y, Niu M, Zhu S, Zhang J, Yan Y, Zhou P, Dai Z, Wu K. Anti-TGF-β/PD-L1 bispecific antibody promotes T cell infiltration and exhibits enhanced antitumor activity in triple-negative breast cancer. J Immunother Cancer. 2022;10(12).
37. Lu Z, Zou J, Li S, Topper MJ, Tao Y, Zhang H, Jiao X, Xie W, Kong X, Vaz M, et al. Epigenetic therapy inhibits metastases by disrupting premetastatic niches. Nature. 2020;579(7798):284–90.
38. Mayoux M, Roller A, Pulko V, Sammicheli S, Chen S, Sum E, Jost C, Fransen MF, Buser RB, Kowanetz M et al. Dendritic cells dictate responses to PD-L1 Blockade cancer immunotherapy. Sci Transl Med. 2020;12(534).
39. Yi M, Niu M, Zhang J, Li S, Zhu S, Yan Y, Li N, Zhou P, Chu Q, Wu K. Combine and conquer: manganese synergizing anti-TGF-β/PD-L1 bispecific antibody YM101 to overcome immunotherapy resistance in non-inflamed cancers. J Hematol Oncol. 2021;14(1):146.
40. Hamon P, Gerbé De Thoré M, Classe M, Signolle N, Liu W, Bawa O, Meziani L, Clémenson C, Milliat F, Deutsch E et al. TGFβ receptor Inhibition unleashes interferon-β production by tumor-associated macrophages and enhances radiotherapy efficacy. J Immunother Cancer. 2022;10(3).
41. Hübner RH, Gitter W, El Mokhtari NE, Mathiak M, Both M, Bolte H, Freitag-Wolf S, Bewig B. Standardized quantification of pulmonary fibrosis in histological samples. Biotechniques. 2008;44(4):507–11. 514– 507.
42. Niu M, Yi M, Wu Y, Lyu L, He Q, Yang R, Zeng L, Shi J, Zhang J, Zhou P, et al. Synergistic efficacy of simultaneous anti-TGF-β/VEGF bispecific antibody and PD-1 Blockade in cancer therapy. J Hematol Oncol. 2023;16(1):94.
43. Wu D, Lim E, Vaillant F, Asselin-Labat ML, Visvader JE, Smyth GK. ROAST: rotation gene set tests for complex microarray experiments. Bioinformatics. 2010;26(17):2176–82.
44. Yang T, Huang T, Zhang D, Wang M, Wu B, Shang Y, Sattar S, Ding L, Liu Y, Jiang H, et al. TGF-β receptor inhibitor LY2109761 enhances the radiosensitivity of gastric cancer by inactivating the TGF-β/SMAD4 signaling pathway. Aging. 2019;11(20):8892–910.
45. Ganesh K, Massagué J. Targeting metastatic cancer. Nat Med. 2021;27(1):34–44.
46. Cohen N, Mundhe D, Deasy SK, Adler O, Ershaid N, Shami T, Levi-Galibov O, Wassermann R, Scherz-Shouval R, Erez N. Breast Cancer-Secreted factors promote lung metastasis by signaling systemically to induce a fibrotic premetastatic niche. Cancer Res. 2023;83(20):3354–67.
47. Chuang CH, Dorsch M, Dujardin P, Silas S, Ueffing K, Hölken JM, Yang D, Winslow MM, Grüner BM. Altered mitochondria functionality defines a metastatic cell state in lung Cancer and creates an exploitable vulnerability. Cancer Res. 2021;81(3):567–79.
48. Baum M, Fallowfield L, Farewell V, Macbeth F, Treasure T. NICE guidelines: management of colorectal cancer metastases. Br J Surg. 2020;107(9):e357.
49. Liang DS, Zhang WJ, Wang AT, Su HT, Zhong HJ, Qi XR. Treating metastatic triple negative breast cancer with CD44/neuropilin dual molecular targets of multifunctional nanoparticles. Biomaterials. 2017;137:23–36.
50. He C, Ding H, Li L, Chen J, Mo X, Ding Y, Chen W, Tang Q, Wang Y. Gold nanoparticles enhance the ability of radiotherapy to induce Immunogenic cell death in glioblastoma. Int J Nanomed. 2023;18:5701–12.
51. Goudot C, Coillard A, Villani AC, Gueguen P, Cros A, Sarkizova S, Tang-Huau TL, Bohec M, Baulande S, Hacohen N, et al. Aryl hydrocarbon receptor controls monocyte differentiation into dendritic cells versus macrophages. Immunity. 2017;47(3):582–e596586.
52. Deng L, Liang H, Xu M, Yang X, Burnette B, Arina A, Li XD, Mauceri H, Beckett M, Darga T, et al. STING-Dependent cytosolic DNA sensing promotes Radiation-Induced type I Interferon-Dependent antitumor immunity in Immunogenic tumors. Immunity. 2014;41(5):843–52.
53. Corrales L, Glickman LH, McWhirter SM, Kanne DB, Sivick KE, Katibah GE, Woo SR, Lemmens E, Banda T, Leong JJ, et al. Direct activation of STING in the tumor microenvironment leads to potent and systemic tumor regression and immunity. Cell Rep. 2015;11(7):1018–30.
54. McLaughlin M, Patin EC, Pedersen M, Wilkins A, Dillon MT, Melcher AA, Harrington KJ. Inflammatory microenvironment remodelling by tumour cells after radiotherapy. Nat Rev Cancer. 2020;20(4):203–17.
55. Rudqvist NP, Charpentier M, Lhuillier C, Wennerberg E, Spada S, Sheridan C, Zhou XK, Zhang T, Formenti SC, Sims JS, et al. Immunotherapy targeting different immune compartments in combination with radiation therapy induces regression of resistant tumors. Nat Commun. 2023;14(1):5146.
56. Li A, Barsoumian HB, Schoenhals JE, Caetano MS, Wang X, Menon H, Valdecanas DR, Niknam S, Younes AI, Cortez MA, et al. IDO1 Inhibition overcomes Radiation-Induced rebound immune suppression by reducing numbers of IDO1-Expressing Myeloid-Derived suppressor cells in the tumor microenvironment. Int J Radiat Oncol Biol Phys. 2019;104(4):903–12.
57. Seifert L, Werba G, Tiwari S, Giao Ly NN, Nguy S, Alothman S, Alqunaibit D, Avanzi A, Daley D, Barilla R, et al. Radiation therapy induces macrophages to suppress T-Cell responses against pancreatic tumors in mice. Gastroenterology. 2016;150(7):1659–e16721655.
58. Hillman GG, Reich LA, Rothstein SE, Abernathy LM, Fountain MD, Hankerd K, Yunker CK, Rakowski JT, Quemeneur E, Slos P. Radiotherapy and MVA-MUC1-IL-2 vaccine act synergistically for inducing specific immunity to MUC-1 tumor antigen. J Immunother Cancer. 2017;5:4.
59. Chen Y, McAndrews KM, Kalluri R. Clinical and therapeutic relevance of cancer-associated fibroblasts. Nat Rev Clin Oncol. 2021;18(12):792–804.
60. Obradovic A, Graves D, Korrer M, Wang Y, Roy S, Naveed A, Xu Y, Luginbuhl A, Curry J, Gibson M, et al. Immunostimulatory cancer-Associated fibroblast subpopulations can predict immunotherapy response in head and neck cancer. Clin Cancer Res. 2022;28(10):2094–109.
61. Nicolas AM, Pesic M, Engel E, Ziegler PK, Diefenhardt M, Kennel KB, Buettner F, Conche C, Petrocelli V, Elwakeel E, et al. Inflammatory fibroblasts mediate resistance to neoadjuvant therapy in rectal cancer. Cancer Cell. 2022;40(2):168–e184113.
62. Denkert C, von Minckwitz G, Darb-Esfahani S, Lederer B, Heppner BI, Weber KE, Budczies J, Huober J, Klauschen F, Furlanetto J, et al. Tumour-infiltrating lymphocytes and prognosis in different subtypes of breast cancer: a pooled analysis of 3771 patients treated with neoadjuvant therapy. Lancet Oncol. 2018;19(1):40–50.
63. Tay C, Tanaka A, Sakaguchi S. Tumor-infiltrating regulatory T cells as targets of cancer immunotherapy. Cancer Cell. 2023;41(3):450–65.
64. Yin Y, Feng W, Chen J, Chen X, Wang G, Wang S, Xu X, Nie Y, Fan D, Wu K, et al. Immunosuppressive tumor microenvironment in the progression, metastasis, and therapy of hepatocellular carcinoma: from bench to bedside. Exp Hematol Oncol. 2024;13(1):72.
65. Shen KY, Zhu Y, Xie SZ, Qin LX. Immunosuppressive tumor microenvironment and immunotherapy of hepatocellular carcinoma: current status and prospectives. J Hematol Oncol. 2024;17(1):25.
66. Saito T, Nishikawa H, Wada H, Nagano Y, Sugiyama D, Atarashi K, Maeda Y, Hamaguchi M, Ohkura N, Sato E, et al. Two FOXP3(+)CD4(+) T cell

subpopulations distinctly control the prognosis of colorectal cancers. Nat Med. 2016;22(6):679–84.
67. Twyman-Saint Victor C, Rech AJ, Maity A, Rengan R, Pauken KE, Stelekati E, Benci JL, Xu B, Dada H, Odorizzi PM, et al. Radiation and dual checkpoint Blockade activate non-redundant immune mechanisms in cancer. Nature. 2015;520(7547):373–7.
68. Mahmood J, Jelveh S, Zaidi A, Doctrow SR, Medhora M, Hill RP. Targeting the Renin-angiotensin system combined with an antioxidant is highly effective in mitigating radiation-induced lung damage. Int J Radiat Oncol Biol Phys. 2014;89(4):722–8.
69. Jenkins RG, Moore BB, Chambers RC, Eickelberg O, Königshoff M, Kolb M, Laurent GJ, Nanthakumar CB, Olman MA, Pardo A, et al. An official American thoracic society workshop report: use of animal models for the preclinical assessment of potential therapies for pulmonary fibrosis. Am J Respir Cell Mol Biol. 2017;56(5):667–79.
70. Tu X, Qin B, Zhang Y, Zhang C, Kahila M, Nowsheen S, Yin P, Yuan J, Pei H, Li H, et al. PD-L1 (B7-H1) competes with the RNA exosome to regulate the DNA damage response and can be targeted to sensitize to radiation or chemotherapy. Mol Cell. 2019;74(6):1215–e12261214.
71. Benci JL, Xu B, Qiu Y, Wu TJ, Dada H, Twyman-Saint Victor C, Cucolo L, Lee DSM, Pauken KE, Huang AC, et al. Tumor interferon signaling regulates a Multigenic resistance program to immune checkpoint Blockade. Cell. 2016;167(6):1540–e15541512.
72. Kim JM, Chen DS. Immune escape to PD-L1/PD-1 Blockade: seven steps to success (or failure). Ann Oncol. 2016;27(8):1492–504.
73. Heras-Murillo I, Adán-Barrientos I, Galán M, Wculek SK, Sancho D. Dendritic cells as orchestrators of anticancer immunity and immunotherapy. Nat Rev Clin Oncol. 2024;21(4):257–77.
74. Wu M, Huang Q, Xie Y, Wu X, Ma H, Zhang Y, Xia Y. Improvement of the anticancer efficacy of PD-1/PD-L1 Blockade via combination therapy and PD-L1 regulation. J Hematol Oncol. 2022;15(1):24.
75. Oh SA, Wu DC, Cheung J, Navarro A, Xiong H, Cubas R, Totpal K, Chiu H, Wu Y, Comps-Agrar L, et al. PD-L1 expression by dendritic cells is a key regulator of T-cell immunity in cancer. Nat Cancer. 2020;1(7):681–91.
76. Fattori S, Le Roy A, Houacine J, Robert L, Abes R, Gorvel L, Granjeaud S, Rouvière MS, Ben Amara A, Boucherit N, et al. CD25high effector regulatory T cells hamper responses to PD-1 Blockade in Triple-Negative breast Cancer. Cancer Res. 2023;83(18):3026–44.
77. Wang H, Yao Z, Kang K, Zhou L, Xiu W, Sun J, Xie C, Yu M, Li Y, Zhang Y, et al. Preclinical study and phase II trial of adapting low-dose radiotherapy to immunotherapy in small cell lung cancer. Med. 2024;5(10):1237–e12541239.
78. Klug F, Prakash H, Huber PE, Seibel T, Bender N, Halama N, Pfirschke C, Voss RH, Timke C, Umansky L, et al. Low-dose irradiation programs macrophage differentiation to an iNOS$^+$/M1 phenotype that orchestrates effective T cell immunotherapy. Cancer Cell. 2013;24(5):589–602.
79. Herrera FG, Ronet C, Ochoa de Olza M, Barras D, Crespo I, Andreatta M, Corria-Osorio J, Spill A, Benedetti F, Genolet R, et al. Low-Dose radiotherapy reverses tumor immune desertification and resistance to immunotherapy. Cancer Discov. 2022;12(1):108–33.

Publisher's note